Hindawi
Scientific Programming
Volume 2021, Article ID 4921276, 9 pages
https://doi.org/10.1155/2021/4921276

Research Article

MRI Images under the Optimized Registration Algorithm for Primary Open Angle Glaucoma Visual Path Damage

Bin Zhou [1] **and Min Chen** [2]

[1]*Department of Ophthalmology, Tonglu First People's Hospital, Hangzhou, China*
[2]*Department of Ophthalmology, Ophthalmologic Center of the Second Affiliated Hospital of Zhejiang University, Hangzhou, China*

Correspondence should be addressed to Bin Zhou; zhoubin@stu.cpu.edu.cn

Received 14 May 2021; Accepted 26 June 2021; Published 5 July 2021

Academic Editor: Gustavo Ramirez

Copyright © 2021 Bin Zhou and Min Chen. This is an open access article distributed under the Creative Commons Attribution License, which permits unrestricted use, distribution, and reproduction in any medium, provided the original work is properly cited.

To explore the impact of different image registration algorithms on the diagnosis of visual path damage in patients with primary open angle glaucoma (POAG), 60 cases of suspected POAG patients were selected as the research objects. Shape-preserving scale invariant feature transform (SP-SIFT) algorithm, scale invariant feature transform (SIFT) algorithm, and Kanade-Lucas-Tomasi (KLT) algorithm were compared and applied to MRI images of 60 POAG patients. It was found that the SP-SIFT algorithm converged after 33 iterations, which had a higher registration speed than the SIFT algorithm and the KLT algorithm. The mean errors of the SP-SIFT algorithm in the rotation angle, X-direction translation, and Y-direction translation were 2.11%, 4.56%, and 4.31%, respectively. Those of the SIFT algorithm were 5.55%, 9.98%, and 7.01%, respectively. Those of the KLT algorithm were 7.45%, 11.31%, and 8.56%, respectively, and the difference among algorithms was significant ($P < 0.05$). The diagnostic sensitivity and accuracy of the SP-SIFT algorithm for POAG were 96.15% and 94.34%, respectively. Those of the SIFT algorithm were 94.68% and 90.74%, respectively. Those of the KLT algorithm were 94.21% and 90.57%, respectively, and the three algorithms had significant differences ($P < 0.05$). The results of MRI images based on the SP-SIFT algorithm showed that the average thickness of the cortex of the patient's left talar sulcus, right talar sulcus, left middle temporal gyrus, and left fusiform gyrus were 2.49 ± 0.15 mm, 2.62 ± 0.13 mm, 3.00 ± 0.10 mm, and 2.99 ± 0.17 mm, respectively. Those of the SIFT algorithm were 2.51 ± 0.17 mm, 2.69 ± 0.12 mm, 3.11 ± 0.13 mm, and 3.09 ± 0.14 mm, respectively. Those of the KLT algorithm were 2.35 ± 0.12 mm, 2.52 ± 0.16 mm, 2.77 ± 0.11 mm, and 2.87 ± 0.17 mm, respectively, and the three algorithms had significant differences ($P < 0.05$). In summary, the SP-SIFT algorithm was ideal for POAG visual pathway diagnosis and was of great adoption potential in clinical diagnosis.

1. Introduction

Glaucoma is a disease characterized by visual field defects and sunken optic nerve atrophy, which can cause serious damage to the patient's visual function. Among blinding eye diseases, the incidence of glaucoma ranks second, second only to cataracts [1]. Among glaucoma patients in China, primary glaucoma accounts for about 87% of the total number of patients, and it mostly occurs in the adult population. At present, glaucoma has caused a great threat to people's vision health.

According to the shape of the patient's chamber angle, primary glaucoma is classified into primary angle closure glaucoma (PACG) and POAG [2]. The onset of POAG is relatively slow. In the early stage, the patient has no clinical symptoms, the fundus is normal, and the vision is not significantly decreased. However, the patient's retinal nerve fiber layer and optic nerve have already been damaged. Therefore, it is very easy to cause misdiagnosis or missed diagnosis to the patient clinically, and it has even developed to a more serious degree when the diagnosis is confirmed. At this time, the damage to the patient's visual function has

been irreversible [3]. At present, the academic community has no clear definite theory on the pathogenesis of POAG. However, it is generally speculated that the increase in the intraocular pressure of the patient at the early stage of the disease causes the pressure of the lamina of the eye to become higher, which compresses the fundus nerve and causes damage, and in turn leads to the loss of the patient's vision [4]. However, such speculation is not fully applicable, and the specific pathogenesis remains to be further explored.

The loss of retinal ganglion cells (RGCs) is the main feature of POAG [5]. In addition, it has been found that POAG may cause damage to the entire visual pathway, including the lateral geniculate nucleus (LGN) and the primary visual cortex (V1) [6], as there are more and more in-depth studies of imaging and histology in recent years. At present, the main diagnostic methods for POAG include optical coherence tomography (OCT), magnetic resonance imaging (MRI), and diffusion tensor imaging (DTI). OCT is currently the main method for glaucoma diagnosis; it can clearly detect the changes in the ganglion cell complex (GCC) and the thickness of the retinal nerve fiber layer (RNFL) in patients, which provides useful information for the diagnosis of glaucoma [7]. In clinical testing, the thinning of RNFL usually determines whether glaucoma nerve damage has occurred. Studies suggested that with the same average visual field defect in patients, glaucoma has more diffuse and severe RNFL loss than nonglaucoma. However, the thinning of RNFL is not unique to glaucoma. Some diseases such as diabetes and hypertension can cause RNFL defects. Therefore, relying solely on OCT can easily lead to misdiagnosis [8]. MRI has a good imaging function for soft tissues, and its multiangle, omnidirectional, noninvasive imaging function is gradually utilized in the diagnosis of eye diseases. One of the main clinical features of glaucoma patients is optic nerve damage, and MRI imaging technology is an effective method to detect optic nerve damage [9]. The image registration algorithm based on traditional mutual information ignores the spatial and directional information of the image and is prone to mismatches. In this research, an optimized image registration algorithm was proposed, namely, the shape-preserving scale invariant feature transform (SP-SIFT) algorithm. This algorithm regards the main phase consistency of the image to be registered as a fuzzy set and introduces the theory of closeness in fuzzy mathematics. Even under the interference of noise, it can achieve high accuracy and strong robustness, which can be applied to MRI image registration [10].

When fundus images are taken, a single image cannot accurately reflect the characteristics of the fundus image due to the limited shooting field of view. Therefore, in clinical diagnosis, it is necessary to take images from multiple angles and then combine the images from various angles as a complete fundus image. After which, the clinician analyzes and compares the images. The progress of some of the images that may cause glaucoma optic nerve damage is tracked, based on which judgments are made. To accomplish these goals, it is necessary to register and combine the patient's fundus images in advance. Therefore, POAG patients were seemed as the research subjects in this work, and the registration accuracy of different registration algorithms and their influence on the diagnosis of POAG visual path damage was analyzed, aiming to provide a reference for the clinical diagnosis of POAG.

2. Materials and Methods

2.1. Research Subjects. In this investigation, 60 patients with suspected POAG who were treated in the hospital from May 2017 to December 2019 were selected as the research subjects. There were 39 males and 21 females, aged 18–70 years, with an average age of 49.6 ± 9.32 years. The control group was set, composed of 60 healthy volunteers. There were 30 males and 30 females, aged 18–65 years old, with an average age of 46 ± 6.85 years old. This study had been approved by the medical ethics committee of the hospital. All subjects were informed of the research objective before the study, and possible injuries were explained during the experiment. The subjects and their families were aware of the research situation and signed the informed consent forms.

Inclusion criteria for the experimental group were defined as patients older than 18 years old and younger than 70 years old, patients with an open anterior chamber angle, patients with intraocular pressure greater than 21 mmHg at least twice, patients without glaucoma visual field defect or other ocular diseases, patients whose visual field was normal for two or more examinations in previous examinations, and patients with complete clinical data.

Exclusion criteria of the experimental group were defined as patients with other ophthalmological diseases, patients with tumors, hypertension, diabetes, cardiovascular, or cerebrovascular diseases, pregnant or lactating women, and patients with metal in the body, which affected the MRI scan.

2.2. Image Preprocessing. At present, the registration algorithms for target images are classified into two types: area-based and feature-based. Feature-based one is more efficient and stable than area-based one, which also has greater advantages in image registration [11]. In this work, the SIFT algorithm based on feature point matching was selected for research.

For multiple multiangle fundus images, to register and stitch them into a complete fundus image, the following steps are generally required: image preprocessing, feature similarity extraction, transformation matrix creation, unified coordinate transformation, and image fusion [12]. Assuming that there are two images, $a(x, y)$ is the image to be registered and $b(x, y)$ is the reference image, the image registration model can be expressed by the following equation.

$$a(x, y) = A[B(b(x, y))]. \quad (1)$$

In equation (1), A represents the one-dimensional gray scale transformation and B represents the two-dimensional spatial coordinate transformation. During registration, the difficulty of image registration will increase due to interference from angle, time, scale, illumination, and noise.

Therefore, before registration, the image to be registered should be smoothed and denoised and contrast enhanced. In this work, the method based on partial differential equations was adopted to denoise the image.

The basic principle of the noise reduction method based on partial differential equations is utilizing the monotonous decreasing function of the image in different directions as its diffusion coefficient [13], and its calculation mode can be expressed by the following equation.

$$\frac{\partial u}{\partial t} = \operatorname{div}\left(g\left(|\nabla u|\right)^2\right)\nabla u. \tag{2}$$

In equation (2), u is the pixel gray level, t is the iteration step size, div is the divergence operator, g is the diffusion coefficient, and ∇u is the image gray gradient. When ∇u becomes smaller, the diffusion coefficient g becomes larger and the image noise is removed. When ∇u becomes larger, the diffusion coefficient g becomes smaller, and the features of the image edge are retained. For the diffusion coefficient g, its function expression is as follows.

$$g\left(|\nabla u|^2\right) = \frac{1}{k|\nabla u|^2 + 1}. \tag{3}$$

After the image is denoised, Gaussian matched filtering is utilized to enhance the image contrast. The change trend of the fundus blood vessel in the cross-section is regarded as a Gaussian curve.

$$G_c(x, y) = \exp\left(-\frac{x^2}{2\sigma^2}\right). \tag{4}$$

In equation (4), $G_c(x, y)$ represents a filtering kernel function of $n \times n$, and σ represents the standard deviation of the Gaussian function along X-axis. After Gaussian filtering, the contrast of the image is well enhanced.

2.3. SP-SIFT Image Registration Algorithm. After the image preprocessing is over, the SIFT algorithm is employed for image similar feature detection. First, the continuously changing scale parameters and image processing information based on different scales are acquired through the Gaussian convolution kernel. The scale space function of the image can be expressed by the following equation.

$$S(x, y, \delta) = G_c(x, y, \delta) \times A(x, y). \tag{5}$$

In equation (5), $S(x, y, \delta)$ represents the scale-space function, $G_c(x, y, \delta)$ represents the Gaussian function, and $A(x, y)$ represents the input image after preprocessing. For a two-dimensional Gaussian convolution kernel $G_c(x, y, \delta)$, its definition can be expressed by the following equation.

$$G_c(x, y, \delta) = \frac{1}{2\pi\sigma^2} e^{\left(-\left(\left(x^2+y^2\right)/2\delta^2\right)\right)}. \tag{6}$$

Difference of Gaussian (DOG) space is adopted to improve the calculation efficiency of stable extreme points during scale space detection. The Gaussian difference scale space expression can be expressed by the following equation.

$$\begin{aligned} f_{\mathrm{DOG}}(x, y, \delta) &= \left[G_c(x, y, k\delta) - G_c(x, y, \delta)\right] \times A(x, y) \\ &= S(x, y, k\delta) - S(x, y, \sigma). \end{aligned} \tag{7}$$

Because of the influence of DOG, it is ensured that the image similarity feature is not affected by light, scale, and noise. The DOG operator can accurately reflect the basic contour features of the input image and is more sensitive to image edges and noise [14], so the precise selection of candidate feature points is achieved by fitting a three-dimensional quadratic function.

For Gaussian difference scale space, the Taylor expansion is as follows.

$$f_{\mathrm{DOG}}(x, y, \delta) = f_{\mathrm{DOG}}(x_0, y_0, \delta) + \frac{\partial f_{\mathrm{DOG}}^t}{\partial x} X + \frac{1}{2} X^t \frac{\partial^2 f_{\mathrm{DOG}}}{\partial x^2} X. \tag{8}$$

In equation (8), (x_0, y_0, δ) represents the local extreme point of the spatial function f_{DOG}, and $X = (x, y, \delta)^T$. The partial derivative of is defined as 0; then, the precise position of the extreme point is shown in the following equation.

$$\widehat{X} = \frac{\partial^2 f_{\mathrm{DOG}}^{-1}}{\partial x^2} \times \frac{\partial f_{\mathrm{DOG}}}{\partial x}. \tag{9}$$

The following equation is acquired by combining equations (7) and (9) and discarding the low contrast points in the image.

$$f_{\mathrm{DOG}}(\widehat{X}) = f_{\mathrm{DOG}}(x, y, \delta) + \frac{\partial f_{\mathrm{DOG}}^T}{2\,\partial x} \widehat{X}. \tag{10}$$

The DOG space curvature characteristic is utilized to remove the edge points of the image. Since the matrix eigenvalues are proportional to the principal curvature of $f_{\mathrm{DOG}}(x, y, \delta)$, for a 2×2 Hessian matrix, there are the following equations.

$$tr(H) = f_{\mathrm{DOG}xx} + f_{\mathrm{DOG}yy} = m + n, \tag{11}$$

$$\det(H) = f_{\mathrm{DOG}xx} f_{\mathrm{DOG}yy} - \left(f_{\mathrm{DOG}xy}\right)^2 = mn. \tag{12}$$

Among which, H is calculated as follows.

$$H = \begin{bmatrix} f_{\mathrm{DOG}xx} & f_{\mathrm{DOG}xy} \\ f_{\mathrm{DOG}xy} & f_{\mathrm{DOG}yy} \end{bmatrix}. \tag{13}$$

In equations (11) and (12), let $m = t \times n$; then, there is the following equation.

$$\frac{tr(H)^2}{\det(H)} = \frac{(m+n)^2}{mn} = \frac{(tn+n)^2}{tn^2} = \frac{(t+1)^2}{t}. \tag{14}$$

When $m = n$, $(t+1)^2/t$ takes the minimum value, and the detected feature points only need to meet the following conditions.

$$\frac{tr(H)^2}{\det(H)} - \frac{(t+1)^2}{t} < 0. \tag{15}$$

The feature points that do not satisfy equation (15) are eliminated.

After the transformation matrix is established, a unified coordinate transformation is performed on the image, and the main direction of the image feature points is determined via gradient histogram. The point (x', y') on the image is defined to represent the feature point scale, and its gradient value $d(x', y')$ can be calculated by the following equation.

$$d(x', y') = \sqrt{[L(x'+1, y') - L(x'-1, y')]^2 + [L(x', y'+1) - L(x', y'-1)]^2}. \quad (16)$$

The direction ϑ can be calculated by the following equation.

$$\vartheta(x', y') = \arctan \frac{L(x', y'+1) - L(x', y'-1)}{L(x'+1, y') - L(x'-1, y')}. \quad (17)$$

The coordinate axis is set as the main direction of the feature point, and finally, the image feature vectors are normalized to obtain the feature points and descriptors of the two registered images. Finally, the images are matched by calculating the similarity of the feature points, and a complete fundus image was obtained.

When multifocus image registration is performed, the different degrees of blurring of the input images may lead to improper selection of the SIFT algorithm scale, resulting in mismatched registration images or reduced similarity [15]. Therefore, the SIFT algorithm is improved to extract the description information in multiple scales to describe the undifferentiated features, which further reduces the mismatching rate.

For a to-be-registered image a and reference image b, the set of their feature points is X^a and X^b, respectively. N_t represents the number of feature points in the feature set t. A point set X^t is adopted to construct the spatial affinity matrix, after the objective function $\varphi(\gamma)$ is minimized, and the following equation is acquired.

$$\varphi(\gamma) = \sum_{m,n} \sum_{i,l} \left\| y_i^m - y_l^n \right\| H_{i,l}^{m,n} + \sum_k \sum_{i,l} \left\| y_i^k - y_l^k \right\| Z_{i,l}^k. \quad (18)$$

For matrix H, the matrix form is adopted to find the optimal solution.

$$\gamma^* = \arg\min_{\gamma^T} tr\left(\gamma^T L \gamma\right). \quad (19)$$

It is supposed that the dimension of the new space coordinate matrix H is d; then, the optimal solution of the above equation is the eigenvector corresponding to the smallest d eigenvalues of the matrix H. By acquiring the corresponding relationship between the feature points of the images a and b, a spatial transformation model of point matching is constructed to realize image registration, as shown in Figure 1.

2.4. Surgical Methods. The RNFL thickness of subjects was detected by OCT. The scanning length was set as 6.0 mm, and the resolution as 640×300. Subject took a sitting position, the lower jaw on dynamic contour tonometer (DCT) scanner rest, the forehead close to forehead bracket, and the eyes fixed on lens marker. The focus knob was adjusted step by step until the fixed visual index was clearly reflected in the eye. Then, a rapid 3D scan of the optic disc was performed, and an annular tomography scan was performed on 640 axial scanning points in the center of the optic disc. The examination results were obtained via the analysis software, and the average RNFL value of the patients was calculated.

MRI data were collected using a 3.0 T MRI scanner with a standard 8-channel cranial coil. Subjects were placed in a supine position with a towel/cushion over the head and the entire brain scanned. Axial T2W1 scanning parameters: 6000/87 ms; layer thickness: 6.0 mm; layer spacing: 1 mm; flip angle: 90°; average frequency: 3 times; matrix: 240×240. A total of 22 layers were collected after the scanning, and the scanning time was 2 minutes and 20 seconds. The scanning data were exported for offline analysis and processing.

2.5. Evaluation Criteria

(i) The benchmark data method and root mean square error (RMSE) were utilized in the accuracy evaluation of the registration algorithm. The benchmark data method took a certain section during MRI scanning as the reference and compared and analyzed the relevant data of the registered image with the reference data. RMSE was utilized to calculate the degree of difference between the image to be registered and the reference image. The calculation equation is as follows.

$$\sigma = \sqrt{\frac{\sum_{i=1}^n \left\| f(a_i') - b_i \right\|^2}{n}}. \quad (20)$$

In equation (20), a_i' and b_i are a pair of matching points in the image to be registered and the reference image, f represents the spatial transformation model, and n represents the logarithm of matching points

(ii) By calculating the sensitivity and accuracy of different registration algorithms for POAG diagnosis, the consistency between the diagnosis results based on different registration algorithms and the expert diagnosis results were compared

(iii) POAG may cause damage to the entire visual pathway. Therefore, the superiority of the algorithm was judged by evaluating the comparison of the cortical thickness tested by different registration algorithms with the true thickness.

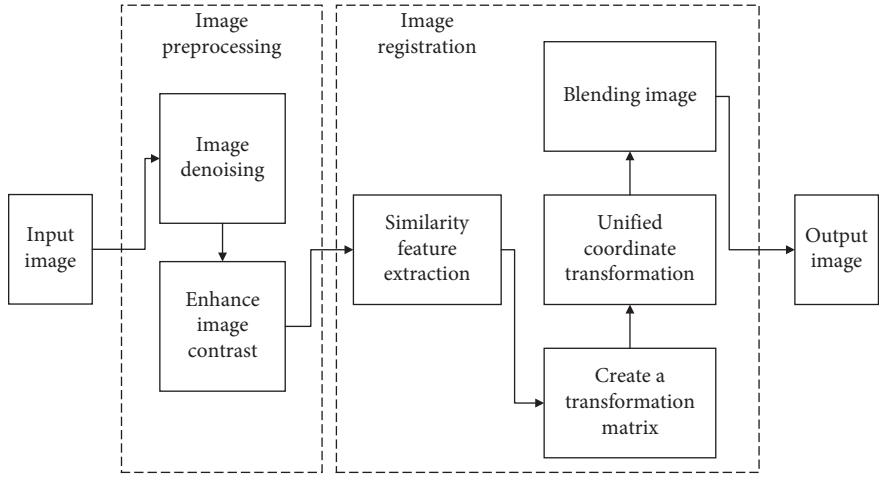

Figure 1: The basic process of image registration.

2.6. Statistical Analysis. All data were processed by SPSS18.0 software. Mean ± standard deviation was how measurement data were illustrated. Differences between groups were tested by the independent sample t-test. $P < 0.05$ indicated that the differences were statistically substantial.

3. Results

3.1. Registration Accuracy Comparison. The 19th slice of the 32nd MRI image of the experimental group was randomly selected for analysis. First, the MRIcro image processing software was employed to rotate the 19th slice, which was the reference image, clockwise by 12°. Then, it moved 8 mm to the right along the X-axis, and moved 10 mm up along the Y-axis to obtain the image to be registered. The SIFT algorithm proposed was employed to simulate the image registration, and the registration results are shown in Figure 2.

The KLT algorithm and the SIFT algorithm were introduced for registration accuracy comparison. The registration parameters are given in Table 1.

From Table 1, the rotation angle of the SP-SIFT algorithm was 11.701°, which was 0.299° different from the actual transformation parameters. The translation amount in the X-axis was 7.581 mm, and the search value of the translation amount in the Y-axis was 4.489 mm, which was 0.419 mm and 0.511 mm apart from the actual transformation parameters, respectively. The rotation angle, X-axis translation, and Y-axis translation of the SIFT algorithm differed from the actual transformation parameters by 0.675°, 0.895 mm, and 0.711 mm, respectively. The rotation angle, X-axis translation, and Y-axis translation of the KLT algorithm differed from the actual transformation parameters by 0.899°, 0.968 mm, and 0.875 mm, respectively. Analysis of the registration parameters showed that the relevant registration parameters of the SP-SIFT algorithm were closer to the standard transformation value, and the registration was more accurate. In terms of convergence speed, since the SP-SIFT algorithm first denoised the image and enhances the contrast, it converged after 33 iterations, which had a higher registration speed than the SIFT algorithm and the KLT algorithm.

Through the multisample registration analysis of the three algorithms, as shown in Figures 3–5, it was found that the SP-SIFT algorithm had 2.11%, 4.56%, and 4.31% in the mean errors of rotation angle, X-axis translation amount, and Y-axis translation, respectively. The mean errors of the SIFT algorithm in the rotation angle, X-axis translation, and Y-axis translation were 5.55%, 9.98%, and 7.01%, respectively. The KLT algorithm had mean errors of 7.45%, 11.31%, and 8.56% in the rotation angle, X-axis translation, and Y-axis translation, respectively. The difference among the three algorithms was statistically significant ($P < 0.05$).

3.2. Comparison of Diagnostic Accuracy Based on Different Registration Methods. 60 patients with suspected POAG underwent routine eye examinations and then OCT testing. Two ophthalmologists diagnosed the results of the examination, and it was found that there was a total of 52 patients that were finally diagnosed with POAG, which was taken as the gold standard for diagnosis. Then, 60 subjects were examined by MRI, and different registration algorithms were employed to register the patient's MRI images, and the diagnosis was made based on the registration results. Table 2 provides that the sensitivity of the SP-SIFT algorithm for POAG diagnosis was 96.15%, the accuracy was 94.34%, the false-positive rate was 5.66%, and the false-negative rate was 3.77%. The diagnostic sensitivity of the SIFT algorithm was 94.68%, the accuracy was 90.74%, the false-positive rate was 9.26%, and the false-negative rate was 5.56%. The diagnostic sensitivity of the KLT algorithm was 94.21%, the accuracy was 90.57%, the false-positive rate was 9.43%, and the false-negative rate was 7.55%. Figures 6 and 7 show the comparison of the diagnosis results of the other two algorithms, and the diagnosis accuracy of the SP-SIFT algorithm was statistically different ($P < 0.05$).

3.3. Cortical Thickness Analysis Based on Different Registration Algorithms. The visual path MRI images of healthy patients in the control group were analyzed, the cortical thickness of the healthy group was calculated, and those

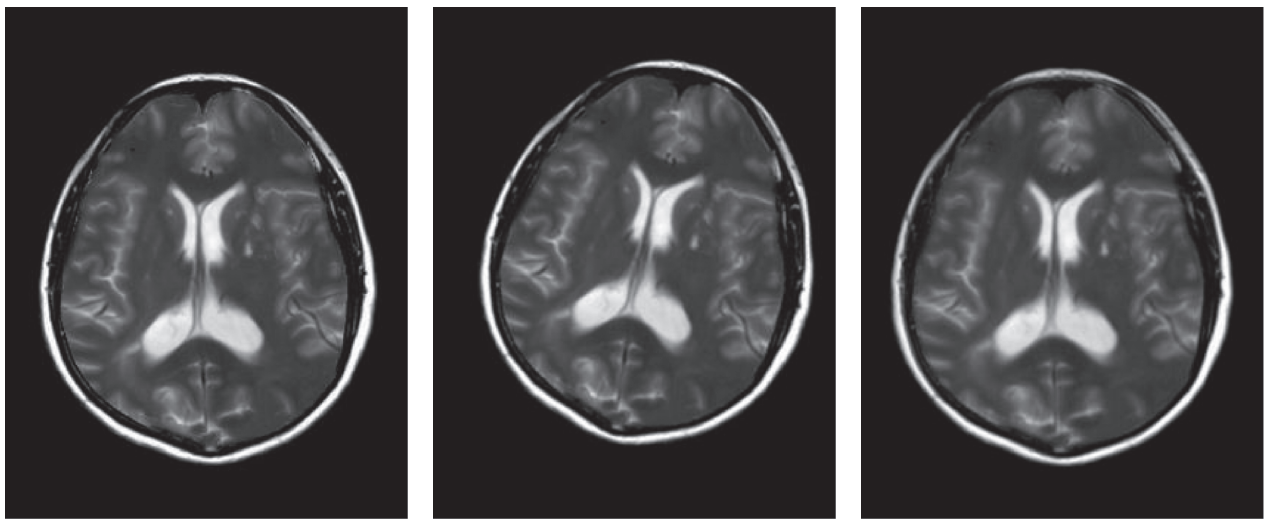

(a) (b) (c)

Figure 2: Registration result of the SP-SIFT algorithm. (a) Reference image. (b) Unregistered image. (c) Image after registration.

Table 1: Registration parameters.

Parameter algorithm	Rotation angle (°)	Translational distance (mm)		Iterations
		X	Y	
Actual parameter	12	8	10	—
KLT	11.101	7.032	4.125	45
SIFT	11.325	8.895	5.711	41
SP-SIFT	11.701	7.581	4.489	33

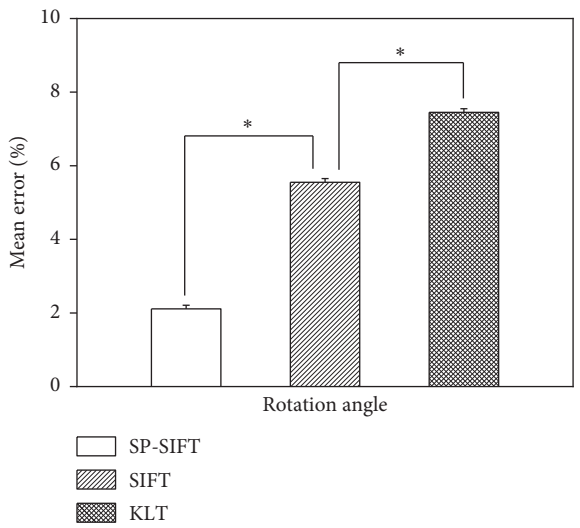

Figure 3: Mean error of rotation angle of different registration algorithms. *The difference was statistically significant ($P < 0.05$).

diagnosed with POAG were taken as the reference standard. Then, the MRI images of 52 patients were analyzed. Based on the results of expert calibration, it was found that the average thickness of the left calcarine sulcus (BA17) cortex was 2.48 ± 0.11 mm, and the average thickness of the right calcarine sulcus was 2.60 ± 0.13 mm (Figure 8). In addition, Figure 9 shows that the patient's left middle temporal gyrus (BA37) and left fusiform gyrus (BA19) also had a small area of cortical thickness thinning, whose average cortical thickness was 2.98 ± 0.18 mm and 3.01 ± 0.17 mm, respectively. In contrast to healthy volunteers, the cortical thickness of POAG patients had a certain degree of thinning. Then, the average thickness of the patient's cortex was calculated according to the MRI images of the patient obtained by different registration algorithms. The analysis results of MRI images based on the SP-SIFT algorithm showed that the average thickness of the cortex of the patient's left calcarine sulcus, right calcarine sulcus, left middle temporal gyrus, and left fusiform gyrus was 2.49 ± 0.15 mm, 2.62 ± 0.13 mm, 3.00 ± 0.10 mm, and 2.99 ± 0.17 mm, respectively. The MRI images based on the SIFT algorithm showed that the average thickness of the cortex of the patient's left calcarine sulcus, right calcarine sulcus, left middle temporal gyrus, and left fusiform gyrus was 2.51 ± 0.17 mm, 2.69 ± 0.12 mm, 3.11 ± 0.13 mm, and 3.09 ± 0.14 mm, respectively. The MRI images based on the KLT algorithm showed that the average thickness of the cortex of the patient's left calcarine sulcus, right calcarine sulcus, left middle temporal gyrus, and left fusiform gyrus was 2.35 ± 0.12 mm, 2.52 ± 0.16 mm, 2.77 ± 0.11 mm, and 2.87 ± 0.17 mm, respectively. The algorithm detection results were compared, and the differences were highly considerable ($P < 0.05$). It was revealed that the analysis result of the patient's cortical

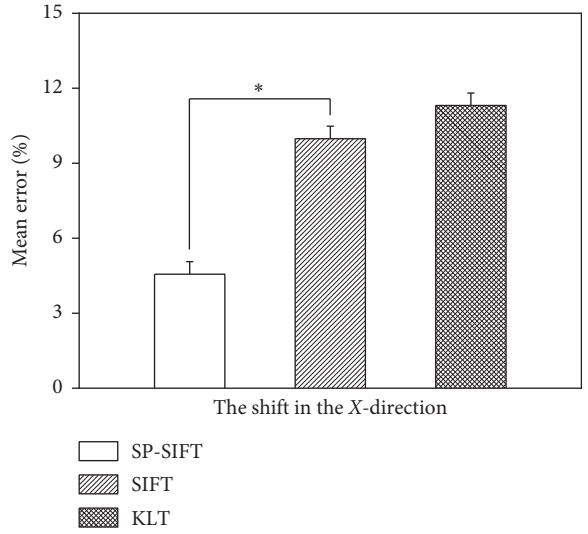

Figure 4: Mean error of translation of different registration algorithms in the X-axis. *The difference was statistically significant ($P < 0.05$).

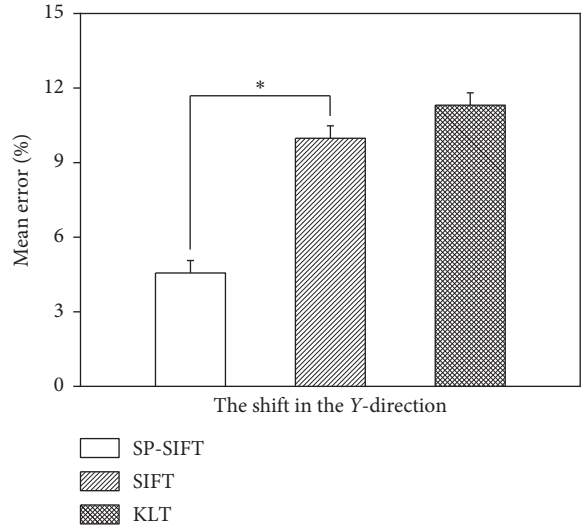

Figure 5: Mean error of translation of different registration algorithms in the Y-axis. *The difference was statistically significant ($P < 0.05$).

Table 2: POAG diagnosis results of different registration algorithms.

Algorithm	Sensitivity (%)	Accuracy (%)	False-positive rate (%)	False-negative rate (%)
SP-SIFT	96.15	94.34	5.66	3.77
SIFT	94.68	90.74	9.26	5.56
KLT	94.21	90.57	9.43	7.55

thickness based on the SP-SIFT algorithm was closer to the true value, and the measurement result was more accurate.

4. Discussion

To explore the effect of different image registration algorithms on the diagnosis of visual path damage in POAG patients, the SIFT registration algorithm was enhanced in this work, and the optimized SP-SIFT registration algorithm was proposed. 60 suspected POAG patients were taken as the research subjects, and a healthy control group was set up. The SP-SIFT algorithm was employed to analyze the accuracy of MRI image registration, the accuracy of POAG diagnosis, and the accuracy of cortical thickness detection. The SIFT algorithm and KLT algorithm were introduced for comparison, and the superiority of the SP-SIFT algorithm for POAG visual path damage diagnosis was verified.

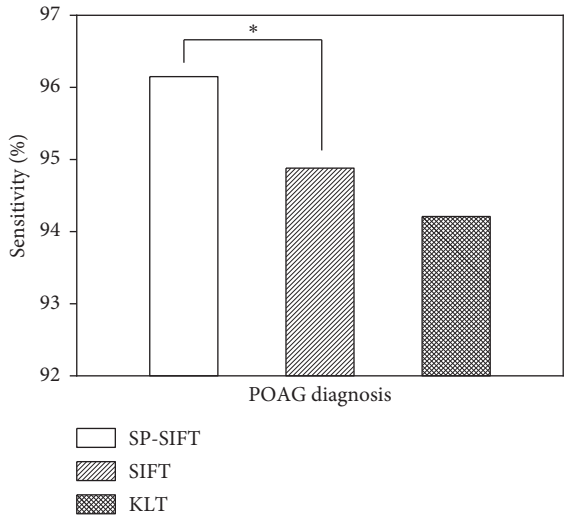

Figure 6: Comparison of sensitivity of different registration algorithms in POAG diagnosis. *The difference was statistically significant ($P < 0.05$).

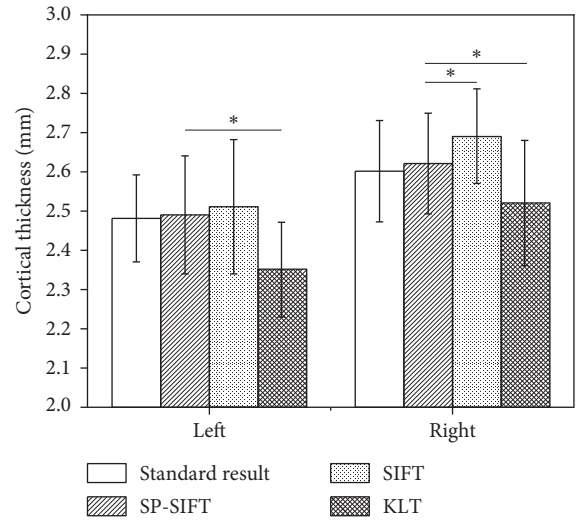

Figure 8: Analysis of the cortical thickness of the calcarine sulcus based on different registration algorithms. *The difference was statistically significant ($P < 0.05$).

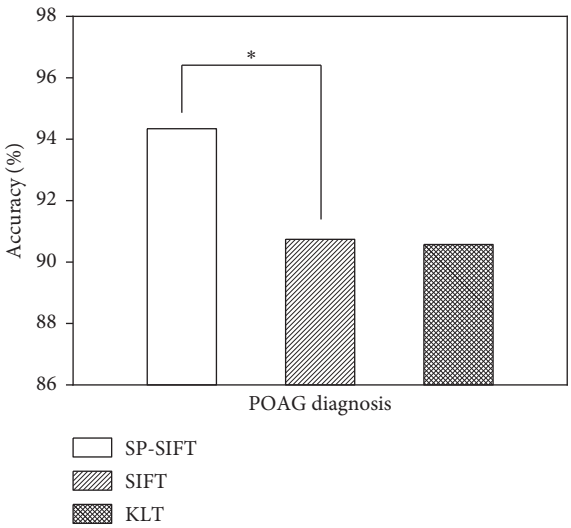

Figure 7: Comparison of accuracy of different registration algorithms in POAG diagnosis. *The difference was statistically significant ($P < 0.05$).

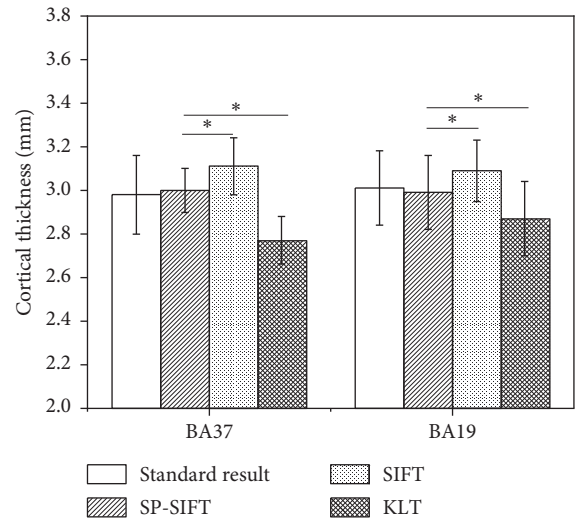

Figure 9: Analysis of the cortical thickness of the left middle temporal gyrus and left fusiform gyrus based on different registration algorithms. *The difference was statistically significant ($P < 0.05$).

It was found that compared with the SIFT algorithm and the KLT algorithm, the relevant registration parameters of the SP-SIFT registration algorithm were closer to the standard transformation value, and the registration was more accurate. Moreover, due to the denoising processing and contrast enhancement of the SP-SIFT algorithm before registration, the SP-SIFT algorithm had a faster registration speed. The suspected POAG patients were diagnosed based on different registration results, and it revealed that the sensitivity of the SP-SIFT algorithm for POAG diagnosis was 96.15%, the accuracy rate was 94.34%, the false-positive rate was 5.66%, and the false-negative rate was 3.77%. The four indicators were better than those of the SIFT algorithm and the KLT algorithm. The diagnostic accuracy of different algorithms was compared, and the difference was statistically remarkable ($P < 0.05$). Finally, by analyzing the cortical thickness of POAG patients, the visual pathway damage of the patients was evaluated. The results showed that compared with the analysis results of MRI images based on the SP-SIFT algorithm, the average thickness of the cortex of the patient's left calcarine sulcus, right calcarine sulcus, left middle temporal gyrus, and left fusiform gyrus was 2.49 ± 0.15 mm, 2.62 ± 0.13 mm, 3.00 ± 0.10 mm, and 2.99 ± 0.17 mm, respectively, which were closer to the expert analysis results. Such results were similar to the results of Wang et al. [16], which showed that the analysis of the patient's cortical thickness based on the SP-SIFT algorithm was accurate, and the diagnosis of POAG visual pathway damage was ideal.

5. Conclusion

This study revealed the impact of different registration algorithms on the accuracy of POAG visual path damage diagnosis. The results showed that the proposed SP-SIFT algorithm had higher registration accuracy and registration speed and had a better diagnosis effect on POAG patients with visual path damage compared with the traditional SIFT algorithm and KLT algorithm. This research provides a theoretical basis for the registration of MRI medical images and provides evidence for the clinical diagnosis of the POAG visual pathway. However, it also has some shortcomings. First of all, the sample size is small, which may lead to reduced statistical reliability. In addition, this MRI examination is the same as before, which adopts the cross-sectional information for study, so it cannot accurately reflect the relationship between visual cortex thickness and POAG disease progression. In the future, research efforts should be strengthened in longitudinal image research.

Data Availability

No data were used to support this study.

Conflicts of Interest

The authors declare that they have no conflicts of interest.

References

[1] H. Youngblood, M. A. Hauser, and Y. Liu, "Update on the genetics of primary open-angle glaucoma," *Experimental Eye Research*, vol. 188, Article ID 107795, 2019.

[2] O. Fekih, H. M. Zgolli, S. Mabrouk, A. Abdejelil, I. Zeghal, and L. Nacef, "Malignant glaucoma management: literature review," *Tunisie Medicale*, vol. 97, no. 8-9, pp. 945–949, 2019.

[3] V. G. Likhvantseva, V. A. Sokolov, O. N. Levanova, and I. V. Kovelenova, "Predicting the probability of development and progression of primary open angle glaucoma by regression modeling," *Vestnik Oftal'mologii*, vol. 134, no. 3, pp. 35–41, 2018, in Russian.

[4] T. N. Malishevskaya, A. R. Yusupov, S. V. Shatskikh, N. A. Antipina, T. S. Klindyuk, and D. S. Bogdanova, "Efficacy and safety of neuroprotection in patients with primary open-angle glaucoma," *Vestnik Oftal'mologii*, vol. 135, no. 2, pp. 83–92, 2019, in Russian.

[5] C. R. Harrell, C. Fellabaum, A. Arsenijevic, B. S. Markovic, V. Djonov, and V. Volarevic, "Therapeutic potential of mesenchymal stem cells and their secretome in the treatment of glaucoma," *Stem Cells International*, vol. 2019, Article ID 7869130, 2019.

[6] X.-Y. Song, Z. Puyang, A.-H. Chen et al., "Diffusion tensor imaging detects microstructural differences of visual pathway in patients with primary open-angle glaucoma and ocular hypertension," *Frontiers in Human Neuroscience*, vol. 12, Article ID 426, 2018.

[7] S. Bertaud, V. Aragno, C. Baudouin, and A. Labbé, "Le glaucome primitif à angle ouvert," *La Revue de Medecine Interne*, vol. 40, no. 7, pp. 445–452, 2019, in French.

[8] P. Brusini, "OCT glaucoma staging system: a new method for retinal nerve fiber layer damage classification using spectral-domain OCT," *Eye*, vol. 32, no. 1, pp. 113–119, 2018.

[9] W. Zhou, E. R. Muir, S. Chalfin, K. S. Nagi, and T. Q. Duong, "MRI study of the posterior visual pathways in primary open angle glaucoma," *Journal of Glaucoma*, vol. 26, no. 2, pp. 173–181, 2017.

[10] M. Fukuda, K. Omodaka, Y. Tatewaki et al., "Quantitative MRI evaluation of glaucomatous changes in the visual pathway," *PLoS One*, vol. 13, no. 7, Article ID e0197027, 2018.

[11] S. Kito, "Outline of deformable image registration for clinical use," *Igaku Butsuri*, vol. 39, no. 1, pp. 7–11, 2019, in Japanese.

[12] R. Y. Wu, A. Y. Liu, J. Yang et al., "Evaluation of the accuracy of deformable image registration on MRI with a physical phantom," *Journal of Applied Clinical Medical Physics*, vol. 21, no. 1, pp. 166–173, 2020.

[13] J. H. Lagergren, J. T. Nardini, G. Michael Lavigne, E. M. Rutter, and K. B. Flores, "Learning partial differential equations for biological transport models from noisy spatio-temporal data," *Proceedings of the Royal Society A: Mathematical, Physical & Engineering Sciences*, vol. 476, no. 2234, Article ID 20190800, 2020.

[14] M. E. Osadebey, M. Pedersen, D. L. Arnold, and K. E. Wendel-Mitoraj, "Blind blur assessment of MRI images using parallel multiscale difference of Gaussian filters," *BioMedical Engineering Online*, vol. 17, no. 1, p. 76, 2018.

[15] B. Rister, M. A. Horowitz, and D. L. Rubin, "Volumetric image registration from invariant keypoints," *IEEE Transactions on Image Processing*, vol. 26, no. 10, pp. 4900–4910, 2017.

[16] J. Wang, T. Li, B. A. Sabel et al., "Structural brain alterations in primary open angle glaucoma: a 3T MRI study," *Scientific Reports*, vol. 6, no. 1, Article ID 18969, 2016.